Korean J. Chem. Eng., 34(2), 320-327 (2017)
DOI: 10.1007/s11814-016-0272-6

pISSN: 0256-1115
eISSN: 1975-7220

Effect of surface composition of Fe catalyst on the activity for the production of high-calorie synthetic natural gas (SNG)

Yong Hee Lee* and Kwan-Young Lee*,,†**

*Department of Chemical and Biological Engineering, Korea University, Anam-dong, Seongbuk-gu, Seoul 02841, Korea
**KU-KIST School of Converging Science & Technology, Korea University, Anam-dong, Seongbuk-gu, Seoul 02841, Korea
(*Received 22 August 2016 • accepted 30 September 2016*)

Abstract−An Fe_2O_3 catalyst was applied to the production of high-calorie synthetic natural gas (SNG). With this catalyst, the product distribution changed as the surface composition of the Fe_2O_3 catalyst changed. The effect of these changes on the catalytic activity was investigated. The active phases of the Fe_2O_3 catalyst were a mixture of low-carbon FeC_x and Fe_3C, which was maintained for 10 h, accompanied by the regeneration of Fe_3O_4. The surface Fe concentration increased after 10 h reaction, and this increased the CO conversion. In addition, the amounts of adsorbed C_2H_4 and C_3H_6 increased, which resulted in an increase in carbon chain growth. The surface concentration of oxygen also increased due to the regeneration of Fe_3O_4, thus reducing the C_3H_6 adsorption strength; in contrast, C_2H_4 adsorption increased, resulting in an enhanced paraffin-to-olefin (p/o) ratio for C_2 hydrocarbons and reduced p/o ratio for C_3 hydrocarbons.

Keywords: Methanation, Fischer-Tropsch, Fe Catalyst, Iron Carbide, Paraffin-to-olefin Ratio

INTRODUCTION

Hydrocarbon fuels are the predominant energy source for modern industry. They can be grouped into three major types: coal as a solid fuel, petroleum as a liquid fuel, and natural gas as a gaseous fuel. In 2014 these three hydrocarbon sources constituted 86.3% of the global primary energy consumption (11,158 million tons of oil equivalent (MTOE)) [1]. However, the use of hydrocarbon fuel is being restricted to reduce the emission of carbon dioxide (CO_2) and thus alleviate global warming. The Paris Agreement recommends that the increase in the average atmospheric temperature should be "well below 2 °C" compared to pre-industrial levels [2]. The International Energy Agency (IEA) has estimated that the average concentration of greenhouse gases should be less than 450 ppm (the 450 Scenario) to suppress any increase in global temperatures to "below 2 °C"; therefore, the contribution of fossil fuels to energy generation should be reduced to 60.4% of the global primary energy demand (9,181 MTOE) by 2040 [3]. Interestingly, only demand for natural gas is expected to increase, from 3,066 MTOE in 2014 to 3,335 MTOE, by 2040; in contrast, the demand for both coal and oil is expected to decrease (3,882 to 2,495 MTOE and 4,211 to 3,351 MTOE, respectively). This implies that the replacement of coal and oil consumption by natural gas will contribute to a reduction in CO_2 emissions and the alleviation of global warming. Among the hydrocarbon fuels, natural gas emits the least amount of CO_2 per unit energy because methane (CH_4), which is the major component of natural gas, has the highest hydrogen per carbon ratio (H/C=4) among hydrocarbons, and because heat is also generated by the oxidation of hydrogen to H_2O. Thus, natural gas is expected to replace coal gradually and to reduce CO_2 emissions; therefore, the demand for natural gas is also expected to increase in the coming decades.

The demand for natural gas was 3,507 billion cubic meter (bcm) in 2013, and, of this, 77.6% (2,721 bcm) was used as fuel: 1,414 bcm for power generation, 758 bcm for building heating, 116 bcm for transport [3]. As a fuel, natural gas has a lower energy density compared to that of oil because it consists of methane and other light gaseous hydrocarbons. The volumetric energy density of liquefied natural gas (LNG) is 20.8-23.6 MJ/L, while that of gasoline is 31.7-34.7 MJ/L [4]. A low energy density is one of the weaknesses of natural gas for use as a fuel; however, its energy density can be enhanced by changing its composition, *i.e.*, increasing the composition of C_2-C_4 hydrocarbons because the energy density of hydrocarbons increases as the carbon number increases. For example, the energy density for liquefied methane at −161.48 °C and 1 atm is 23.4 MJ/L, while that for ethane and propane is 32.6 and 35.5 MJ/L, respectively (calculated based on the data from NIST chemistry webbook [5]). Therefore, the energy density of natural gas is determined by the composition of gaseous light hydrocarbons (C_1-C_4).

However, the energy density of natural gas continuously decreases (the energy density of natural gas is expressed as the heating value under atmospheric conditions). Generally, the heating value of LNG is greater than that of pipeline natural gas (PNG): the standard heating value for Japan which imports LNG is 45-46 MJ/Nm^3 [6,7], while the average heating value of natural gas for U.S. and Russia, which deliver natural gas by pipeline, is 33.8-38.8 MJ/Nm^3 [8-10]. The lower heating value of PNG results from the separation of the C_2-C_4 components to prevent the formation of hydrocarbon hydrates that can damage the pipeline during transport [11]. This sepa-

†To whom correspondence should be addressed.
E-mail: kylee@korea.ac.kr
‡This article is dedicated to Prof. Sung Hyun Kim on the occasion of his retirement from Korea University.

ration of C_2-C_4 components significantly lowers the heating value of the entire natural gas system because the traded amount of PNG (663.9 bcm) was almost twice as great as that of LNG (333.3 bcm) in 2014 [1]. In addition, because of the increased demand for LNG, suppliers have lowered the heating value of LNG comparable to that of PNG, and C_2-C_4 hydrocarbons separated from LNG are used for the production of light olefins or liquefied petroleum gas (LPG). As a result, the average heating value of natural gas has decreased. This decrease in the heating value of natural gas causes a serious problem, especially in Japan and South Korea, whose standard heating value is set at the high heating value of LNG (42.7-45 MJ/Nm^3). Currently, LPG (a mixture gas of propane and butane) is added to low-calorie natural gas to enhance the heating value. However, the amount of consumed LPG and the material cost for the LPG mixing process increases significantly as the average heating value decreases. The price of LPG strongly depends on the oil price; then the role of natural gas as the substitute for oil is restricted if heat is only added by LPG. Thus, another high-calorie gas is needed to replace LPG.

There are several reactions to produce gaseous light hydrocarbons in the C_2-C_4 range: direct synthesis of LPG, iso-synthesis, and light olefin synthesis. LPG synthesis reactions selectively produce propane and butane directly from synthesis gas (a H_2/CO mixture), whereas the iso-synthesis reaction is a more selective reaction producing isobutane or isobutene. LPG synthesis and iso-synthesis achieve low CO conversions (around 75% and 20-35%, respectively) and high CO_2 selectivities (40-50%) because these reactions are at lower H_2/CO ratios (2 for LPG synthesis and 1 for iso-synthesis) than the stoichiometric ratio (2.33 for C_3H_8 and 2.25 for C_4H_{10}) to suppress the formation of CH_4 [12-25]. Light olefin synthesis reactions, or the Fischer-Tropsch to olefins (FTO) process, is part of the Fischer-Tropsch reaction that is carried out at temperatures (300-400 °C) higher than that for the conventional Fischer-Tropsch reaction (220-250 °C). Reaction at these higher temperatures restricts the growth of the carbon chain. Iron catalysts have been used in this reaction rather than cobalt catalysts because Fe catalysts have lower methane selectivities and higher olefin selectivities, even at temperatures greater than 300 °C, due to their lower hydrogenation activities compared to Co catalysts [26]. At greater than 70% CO conversion with low C_{5+} selectivity below 20%, the C_2-C_4 hydrocarbon selectivity is between 25-45% and the olefin-to-paraffin (o/p) ratio in the C_2-C_4 range was between 2-16 with CO_2 selectivities between 35 and 60% [27-29].

The three reactions mentioned above were at H_2/CO ratios of 1 to 2 to suppress the formation of CH_4. However, the lack of H_2 in the feed syngas resulted in low CO conversion, high CO_2 selectivity, and high olefin selectivity in the FTO case, which lowered the yield and the heating value of the high-calorie gas (the heating value of olefin is lower than that of paraffin with equal carbon number). Because the stoichiometric H_2/CO ratio for methanation is 3, CH_4 selectivity increases as H_2/CO ratio increases, which is not favored in light hydrocarbon synthesis or the Fischer-Tropsch reaction. However, CH_4 formation is not a serious problem when mixing with natural gas. Therefore, the H_2/CO ratio in the feed syngas should be increased above 2 to enhance CO conversion and paraffin selectivity and to lower CO_2 selectivity.

In conventional methanation reactions at H_2/CO=3, nickel catalysts that are highly selective for CH_4 are used [30,31], and the formation of C_{2+} hydrocarbons is suppressed. To enhance C_2-C_4 hydrocarbon selectivity in methanation conditions, Co or Fe must be used as the catalytic component instead of Ni. Co-based catalysts have been used for this so-called "high-calorie methanation" by Inui et al., and high-calorie synthetic natural gas (SNG) has been successfully produced from coke oven gas using a Co-Mn-Ru/Al_2O_3 catalyst [32]. In our previous publications, we found that Co-Mn-Ru/Al_2O_3 also produces high-calorie SNG with a heating value between 43.8 and 48.6 MJ/Nm^3 from synthesis gas [33,34]. However, a much greater heating value of the produced SNG is needed to enhance the heating value of the low-calorie gases by mixing. Therefore, we examined the activity of Fe-based catalysts in the production of high-calorie SNG, which have much higher C_2-C_4 hydrocarbon selectivities compared to that of the Co catalyst, as mentioned above. In our previous publication, carburized Fe-Zn catalysts achieved CO conversions of over 95% and C_2-C_4 selectivities between 38 and 41%, producing SNG with a heating value of more than 56 MJ/Nm^3 [34].

The active phase of Fe catalysts in CO hydrogenation is a mixture of iron oxide and iron carbide, and the composition differs depending on the reaction conditions. In the Fischer-Tropsch reaction, the active phases of the Fe catalyst are a mixture of magnetite (Fe_3O_4) and various iron carbides such as χ-Fe_5C_2 and ε'-$Fe_{2.2}C$ [35-37]. In the production of high-calorie SNG, the active phase for the Fe catalyst is also a mixture of Fe_3O_4 and iron carbides, but relatively less-carburized iron carbides are formed: Fe_3C and low-carbon FeC_x (x<1/3) [34]. The reduction in the degree of carburization results in a reduction in the carbon chain growth because the decrease in surface carbon results in a decrease in the formation of ketenylidene species (C=C=O), key intermediates for carbon chain growth [38,39]. Therefore, low-carbon iron carbide restricts the formation of higher hydrocarbons (*i.e.*, over C_5) and enhances C_2-C_4 gaseous hydrocarbon formation.

In this study, the surface properties of low-carbon iron carbides (low-carbon FeC_x and Fe_3C) and their influence on the high-calorie SNG production activity were studied using an unpromoted Fe_2O_3 catalyst. The Fe_2O_3 catalyst was reduced and carburized using dilute CO gas at 400 °C, a temperature at which low-carbon iron carbides are formed. The activity for the production of high-calorie SNG was evaluated regarding CO conversion, hydrocarbon distribution, chain growth probability (α), and the paraffin-to-olefin ratio in the C_2-C_4 range. Because the activity changed with reaction stream time, the reasons for the activity change were investigated by comparing the properties of Fe_2O_3 after CO reduction and after 10 h reaction time. The surface composition and the electronic structure of Fe_2O_3 catalyst were measured by X-ray photoelectron spectroscopy (XPS), and the change of the surface properties due to the change in the surface composition was examined by various temperature programmed desorption (TPD) techniques.

EXPERIMENTAL

1. Catalyst Preparation

The Fe_2O_3 catalyst was prepared by a conventional precipitation

method. The metal precursor, $Fe(NO_3)_3 \cdot 9H_2O$ (Sigma-Aldrich), was dissolved in deionized water, and the total concentration of the metal precursors was 1 M. Before the metal precursor solution was added, the temperature of the deionized water (100 mL) contained in the three-neck flask was adjusted to 80 °C. Then, the metal precursor solution was added to the flask dropwise at a rate of 2 mL/min. The pH was maintained at 7 using a 1 M solution of K_2CO_3 (Sigma-Aldrich) while adding the precursor solution. After being aged for 2 h, the precipitate was washed with 6 L of deionized water and dried at 110 °C overnight. The dried precipitate was calcined at 550 °C for 5 h under static air.

2. Characterization

For CO temperature programmed reduction (CO-TPR) analysis, we used a BELCAT-M-77 instrument (BEL Japan Inc.). Before analysis, samples were purged at 110 °C for 1 h under a 30 mL/min flow of He gas. TPR data were recorded from 60 °C to 800 °C at a heating rate of 5 °C/min under a 30 mL/min flow of 8% CO/He mixture gas. Temperature programmed desorption analysis was performed using the same instrument. C_2H_4 and C_3H_6 (adsorbates) were adsorbed on a sample at 35 °C for 30 min using 10% C_2H_4/He and 10% C_3H_6/He mixture gas, respectively. Physisorbed adsorbate molecules were removed at 120 °C for 1 h by pure He gas flow at a rate of 30 mL/min. TPD data were recorded between 120 °C to 810 °C at a rate of 5 °C/min under a flow of pure He gas at 30 mL/min.

X-ray diffraction (XRD) patterns were obtained using a D/MAX-2500/PC diffractometer (Rigaku) operated at 40 kV and 100 mA with Cu-Kα1 irradiation (λ=0.15406 nm). All samples were mixed with an internal standard (Si powder at 10 wt%). The diffraction data were collected between 20° to 50° (2θ) at a rate of 1.5°/min. X-ray photoelectron spectroscopy analysis was performed on an ESCALAB 250Xi X-ray monochromator (Thermo-Scientific) using the monochromatic Al-Kα line as the X-ray source.

3. Activity Tests

The activity tests were performed in a continuous fixed bed reactor using 0.15 g of the catalyst material. The catalyst was sieved to obtain particle sizes in the range of 53 μm to 75 μm. The catalyst was packed in the middle of a 400 mm tubular stainless-steel reactor (I.D.=9.5 mm) and, before the reaction, reduced (carburized) at 400 °C for 3 h using 8% CO/He gas. After the reduction, the feed gas, which was composed of $CO : H_2 : N_2 = 24 : 72 : 4$ (H_2/CO ratio=3), was introduced in the reactor at a flow rate of 15 mL/min. The reactor was pressurized to 1 MPa by the feed gas using back pressure regulator (TESCOM, 26-1700 series), and the reaction pressure was maintained at 1 MPa over the course of the reaction.

The compositions of the feed and product gases were analyzed by gas chromatography (Younglin YL6500GC). Hydrocarbon components were separated by HP plot Q column, which was connected to flame ionization detectors (FID), whereas the other gases (N_2, CO, and CO_2) were separated by Carboxen 1000 columns, which were connected to a thermal conductivity detector (TCD). Nitrogen was used as the internal standard to determine the flow rate and the gas compositions.

CO conversion and product selectivity were calculated using Eqs. (1)-(3). The chain growth probability (α) was determined from an Anderson-Schulz-Flory (ASF) plot using Eq. (4) [40,41].

$$\text{CO conversion (carbon mole \%)} = \left(1 - \frac{\text{CO in the product gas (mol/min)}}{\text{CO in the feed gas (mol/min)}}\right) \times 100 \quad (1)$$

$$\text{Selectivity for hydrocarbon with carbon number n (carbon mole \%)} = \frac{n \times C_n \text{ hydrocarbon in the product gas (mol/min)}}{(\text{total carbon} - \text{unreacted CO}) \text{ in the product gas (mol/min)}} \times 100 \quad (2)$$

$$\text{Selectivity for carbon dioxide (carbon mole \%)} = \frac{CO_2 \text{ in the product gas (mol/min)}}{(\text{total carbon} - \text{unreacted CO}) \text{ in the product gas (mol/min)}} \times 100 \quad (3)$$

The Anderson-Schulz-Flory plot

$$\log(W_n/n) = n\log\alpha + \log[(1-\alpha)^2/\alpha], \quad (4)$$

where W_n is the mass fraction of hydrocarbon containing n carbon atoms.

For convenience, Fe_2O_3 after 10 h reaction is labeled as 'Fe_2O_3-R,' and Fe_2O_3 after 10 h reaction is labeled as 'Fe_2O_3-AR.'

RESULTS AND DISCUSSION

1. The Formation of Low-carbon Iron Carbides

Fig. 1 shows the CO-TPR and XRD results for the Fe_2O_3 catalyst. In CO-TPR, CO_2 is generated when a sample is reduced by CO. Due to the difference in thermal conductivity between CO and CO_2, both positive and negative peaks appear according to the molar ratio of produced CO_2 and consumed CO ($\Delta CO_2/\Delta CO$). If this ratio is smaller than approximately 0.95, a negative peak appears, and a positive peak appears in opposite cases. Details of the reduction and carburization steps for the Fe catalysts have been reported in our previous publications by comparing CO-TPR curves and XRD data [34,42], and similar results were obtained in this study.

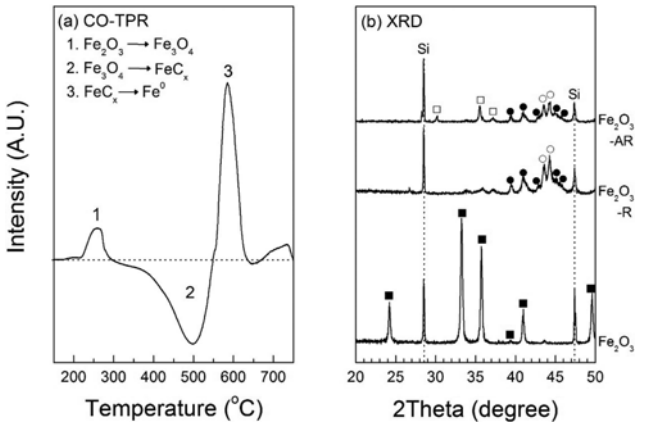

Fig. 1. (a) CO-TPR curve of unreduced Fe_2O_3 and (b) XRD results of unreduced Fe_2O_3, Fe_2O_3 reduced by an 8% CO/H_2 mixture gas at 400 °C for 3 h (Fe_2O_3-R), and Fe_2O_3 after 10 h reaction (Fe_2O_3-AR): ■ α-Fe_2O_3; □ Fe_3O_4; ○ low-carbon FeC_x; ● Fe_3C.

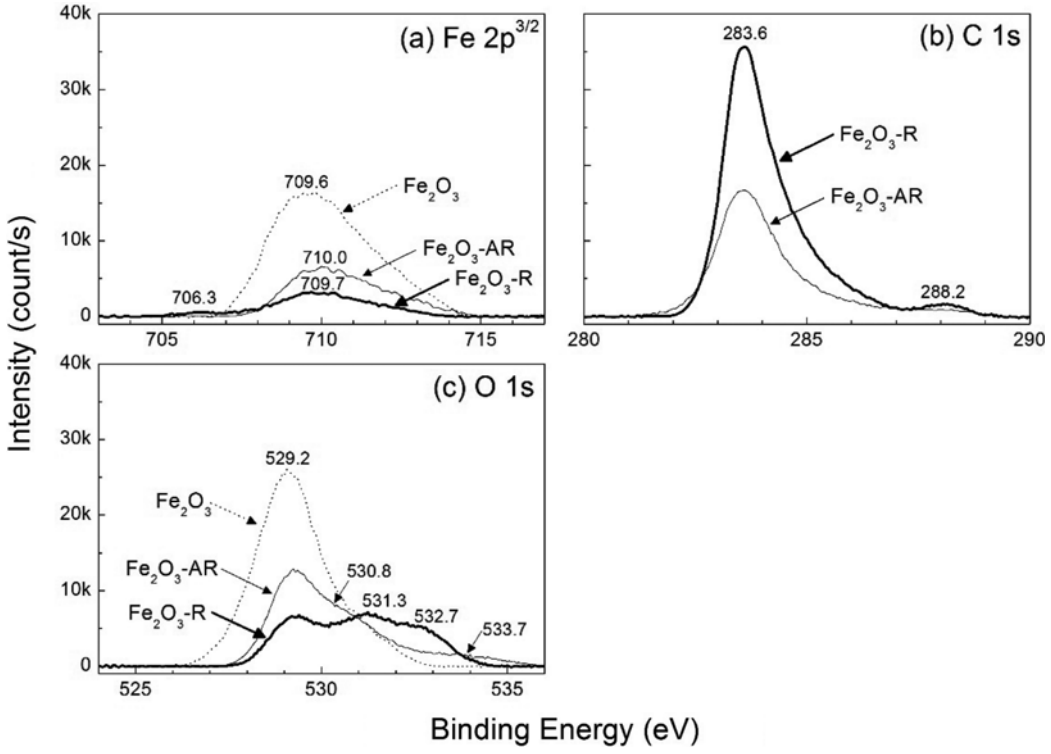

Fig. 2. The binding energy of (a) Fe 2p core electrons, (b) C 1s electrons and (c) O 1s electrons measured by XPS.

As shown in the XRD results in Fig. 1(b), unpromoted Fe_2O_3 was composed of α-Fe_2O_3 (hematite) after calcination. During reduction by CO, α-Fe_2O_3 was first reduced to Fe_3O_4 (magnetite). $\Delta CO_2/\Delta CO$ ratio was 1 (Eq. (5)); thus, a positive peak appeared at 260 °C (peak 1 in Fig. 1(a)).

$$Fe_2O_3+\frac{1}{3}CO\rightarrow\frac{2}{3}Fe_3O_4+\frac{1}{3}CO_2 \quad (5)$$

Fe_3O_4 was carburized to iron carbides (FeC_x) between 300 and 550 °C. $\Delta CO_2/\Delta CO$ ratio is below 0.95 when x is over 0.074 (Eq. (6)). Therefore, a negative peak appeared due to the carburization of Fe_3O_4 (peak 2 in Fig. 1(a)), because x is larger than 0.074 in iron carbides (x=1/3 for Fe_3C, x=0.075 for $Fe_{1.86}C_{0.14}$).

$$Fe_3O_4+(6x+4)CO\rightarrow 3FeC_x+(3x+4)CO_2 \quad (6)$$

Finally, iron carbides were reduced to metallic Fe (peak 3 in Fig. 1(a)), but the exact sequence of this reduction is not clear.

After CO reduction at 400 °C for 3 h, α-Fe_2O_3 was carburized to the mixture of low-carbon FeC_x (C/Fe<1/3) and Fe_3C (Fe_2O_3-R in Fig. 1(b)). The peak for low-carbon FeC_x appeared at 43.4°, and 44.2° were the peaks for $Fe_{1.86}C_{0.14}$ (C/Fe=0.075, JCPDS #44-1289) and $Fe_{1.945}C_{0.055}$ (C/F=0.028, JCPDS #44-1290), respectively. However, the exact composition of these iron carbides is not clear; thus, we labeled this as the low-carbon FeC_x. After 10 h reaction, the major Fe species were low-carbon FeC_x and Fe_3C, but Fe_3O_4 (Fe_2O_3-AR in Fig. 1(b)) was also formed by the re-oxidation of a small portion of iron carbide.

As a result, low-carbon iron carbides were successfully generated by CO reduction at 400 °C. Furthermore, the low-carbon iron carbides were maintained after 10 h reaction time accompanied by the regeneration of a small portion of Fe_3O_4.

2. The Surface Composition of the Fe_2O_3 Catalyst

XPS analysis on the surface of Fe_2O_3 catalyst was carried out. First, the XPS results for Fe $2p^{3/2}$ electrons in Fe_2O_3, Fe_2O_3-R, Fe_2O_3-AR are presented in Fig. 2(a). The binding energies of Fe $2p^{3/2}$ electrons in Fe oxides (Fe_2O_3, Fe_3O_4, and FeO) and Fe carbide (Fe_3C) have similar values, between 708.1-711.5 eV [43]. Therefore, the peaks observed at 709.6-710.0 eV are due to Fe 2p electrons in Fe oxide and Fe carbide. Aside from these peaks, only one peak appeared at a lower binding energy (706.3 eV) in the XPS result for Fe_2O_3-R. The binding energy for Fe $2p^{3/2}$ electrons in metallic Fe is, generally, between 706.5 eV and 707.1 eV. Thus, low-carbon FeC_x had a metal-like electron structure due to the lack of bonded carbon after carburization [42]. However, this metal-like Fe disappeared at the surface of the catalyst after 10 h reaction (Fe_2O_3-AR),

Table 1. The concentration of C, O, and Fe on the surface of the Fe_2O_3 catalyst measured by XPS

Element	Atomic concentration on the surface (%)		
	Fe_2O_3[a]	Fe_2O_3-R[b]	Fe_2O_3-AR[c]
C	-	84.0	68.0
O	69.5	13.7	25.3
Fe	30.5	2.3	6.7

[a]Fe_2O_3 after calcination at 550 °C for 5 h
[b]Fe_2O_3 after CO reduction at 400 °C for 3 h
[c]Fe_2O_3 after 10 h reaction

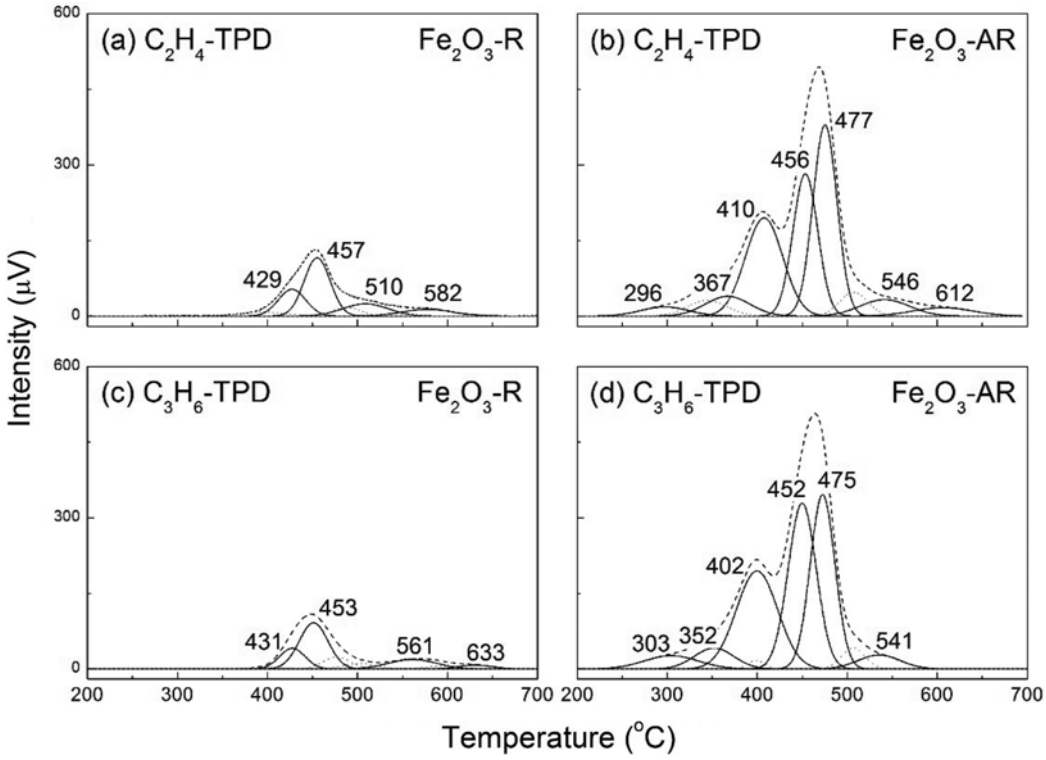

Fig. 3. C_2H_4 and C_3H_6 TPD analysis results for Fe_2O_3-R and Fe_2O_3-AR.

although the bulk crystallite of low-carbon FeC_x in the XRD pattern (Fe_2O_3-AR in Fig. 1(b)) did not disappear. This result suggests that Fe and C were not uniformly distributed right after the carburization, and catalyst uniformity was achieved after 10 h reaction. In Table 1, the atomic concentration of each component on the surface of the catalyst measured by XPS analysis is presented. The surface concentration of carbon decreased from 84.0% (Fe_2O_3-R) to 68.0% (Fe_2O_3-AR) and that of Fe increased from 2.3% (Fe_2O_3-R) to 6.7% (Fe_2O_3-AR) after 10 h reaction. Therefore, metal-like Fe on the surface of the catalyst was formed because the incorporation of carbon was limited during carburization, disappearing after 10 h reaction. In contrast, the increase in the surface concentration of oxygen (from 13.7% to 25.3%) resulted from the regeneration of Fe_3O_4.

The C 1s and O 1s XPS spectra are shown in Fig. 2(b) and 2(c), respectively. The binding energy of the C 1s electrons in Fe_3C is 283.6 eV, and values determined in other iron carbides have similar values (283.2-283.9 eV) [43]. Thus, the peaks at 283.6 eV are diagnostic of C 1s electrons in iron carbides. Another peak at 288.2 eV appeared only in the spectrum of Fe_2O_3-R, and this is suggestive of C 1s electrons in iron carbonate ($Fe(CO)_5$, 288.0 eV) [43]. In Fig. 2(c), the XPS results for O 1s electrons are presented. The first peak at 529.2 eV is characteristic of O 1s electrons in iron oxides; for example, O 1s electrons in Fe_2O_3, Fe_3O_4, and FeO have similar binding energies, ranging from 529.1 eV to 530.3 eV. In Fe_2O_3-R, additional peaks at 531.8 eV, and 532.7 eV appeared, possibly arising from O 1s electrons in carbonate (CO); however, we could not clearly determine the origin of this peak. Furthermore, after 10 h reaction, these two peaks disappeared, and the iron oxide peak intensity increased. Fe_3O_4 has a spinel structure and contains two different Fe species (Fe^{2+} and Fe^{3+}). Thus, a shoulder peak at 530.8 eV appeared. The peak at 533.7 eV might represent O 1s electrons in H_2O.

In summary, the surface compositions of Fe_2O_3-R and Fe_2O_3-AR are different. Carbon is incorporated in the interior of the catalyst during the 10 h reaction course, and, as a result, the carbon concentration at the surface decreased and the iron concentration increased. The metal-like Fe in Fe_2O_3-R and also iron carbonate disappeared in Fe_2O_3-AR.

3. C_2H_4 and C_3H_6 Adsorption on Fe_2O_3 Catalyst

C_2H_4- and C_3H_6-TPD results of Fe_2O_3-R and Fe_2O_3-AR are shown in Fig. 3, and the adsorbed amounts of each adsorbate on the surface of Fe_2O_3 catalyst are listed in Table 2. The adsorbed amount of C_2H_4 (0.050 mmol/g) was greater than that of C_3H_6 (0.033 mmol/g) on Fe_2O_3-R. The adsorbed amount was much larger on the surface of Fe_2O_3-AR for both C_2H_4 (0.215 mmol/g) and C_3H_6 (0.169 mmol/g) than that on Fe_2O_3-R. The increase of the adsorbed amount

Table 2. The adsorbed amount of each adsorbate on Fe_2O_3-R and Fe_2O_3-AR in TPD analysis

Adsorbate	Adsorbed amount (mmol/g)[a]	
	on Fe_2O_3-R	on Fe_2O_3-AR
C_2H_4	0.050	0.215
C_3H_6	0.033	0.169

[a]Adsorbed amount of each adsorbate was calculated based on the area of the peaks in Fig. 3

Table 3. High-calorie SNG production activity of the Fe_2O_3 catalyst

Catalyst	Time on stream	CO conversion (%)	Selectivity (%)				α^a
			CH_4	C_2-C_4	C_{5+}	CO_2	
Fe_2O_3-R	0.5 h	93.6	24.2	35.7	9.6	30.5	0.18
Fe_2O_3-AR	10 h	95.2	22.3	35.5	11.5	30.6	0.21

[a] α values were calculated based on the Anderson-Flory-Shultz distribution in the C_1-C_6 range

of olefin might be caused by the increased surface Fe concentration (see XPS results in Table 1). In addition, electron-rich sites suppress the adsorption of olefins and promote their desorption because electron-rich sites repulse electrons in the olefin double bond [44]. This result implies that the disappearance of electron-rich, metal-like Fe after 10 h reaction promoted the adsorption of olefins.

For C_2H_4, the strength of the adsorption also increased on the surface of Fe_2O_3-AR. The temperatures of the desorption peaks observed at temperatures greater than 500 °C increased by about 30 °C (*i.e.*, from 510 °C to 546 °C and 582 °C to 612 °C). In contrast, for C_3H_6, the strength of the adsorption decreased on Fe_2O_3-AR. One of the two peaks observed at over 500 °C disappeared (633 °C), and the other peak shifted to a lower temperature (541 °C from 561 °C). The electrons in the double bond of C_3H_6 are delocalized toward the third carbon compared to those of C_2H_4 because carbon has higher electron negativity than hydrogen. Thus, if the electron density of the surface increases, C_3H_6 adsorption is suppressed due to the repulsion between the methyl group and the surface oxygen. For Fe_2O_3-AR, the surface concentration of oxygen increased due to the regeneration of Fe_3O_4. In addition, the electron density in the oxygen atoms of Fe_2O_3-AR might be higher than that on Fe_2O_3-R because the carbonate or hydroxide species on Fe_2O_3-AR disappeared, lowering the electron density of the oxygen species. As a result, the strength of C_3H_6 adsorption was weakened. In contrast, the strength of C_2H_4 adsorption increased, implying that the interaction between hydrogen and surface oxygen promoted C_2H_4 adsorption.

As a result, the adsorbed amount of C_2H_4 was much larger than that of C_3H_6 on both Fe_2O_3-R and Fe_2O_3-AR. The strength of the adsorption for C_2H_4 and C_3H_6 was similar on Fe_2O_3-R. However, the adsorption strength for C_2H_4 became stronger on Fe_2O_3-AR, while that for C_3H_6 became weaker due to the increase of the surface oxygen concentration.

4. The High-calorie SNG Production Activity

The activity results of Fe_2O_3 catalyst are listed in Table 3. The initial activity (after 0.5 h) is the activity of Fe_2O_3-R, and the activity at 10 h in the reaction is the activity of Fe_2O_3-AR. First, CO conversion increased from 93.6% for Fe_2O_3-R to 95.2% for Fe_2O_3-AR after 10 h reaction, and this results from the increase in surface Fe concentration, which was 6.7% on Fe_2O_3-AR, having increased from 2.3% on Fe_2O_3-R. The CO adsorption energy on iron carbide surface is the largest of surfaces with carbon vacancies (−134 to −131 kJ/mol) when compared to non-vacant (fully carburized) surfaces (−112 kJ/mol) and carbon-free surfaces (−129 to −126 kJ/mol) [45]. This observation implies that an increase in the Fe concentration accompanied by a decrease in carbon concentration enhances CO adsorption, resulting in increased CO conversion.

Concerning product selectivity, the C_n hydrocarbon (n≥2) selectivity and α value increased from 45.3% to 47.0% and 0.18 to 0.21 after 10 h reaction, respectively. Consequently, the carbon chain growth was enhanced in Fe_2O_3-AR compared to Fe_2O_3-R. The increase in the carbon chain growth on Fe_2O_3-AR was related to an increase in the amount of adsorbed C_2H_4 and C_3H_6. The re-adsorption of olefins during the Fischer-Tropsch reaction increases carbon chain growth by reinsertion of hydrocarbon species into the chain growth reaction [46,47]. Due to the increase in the surface Fe concentration, the adsorbed amounts of C_2H_4 and C_3H_6 were 4.3 and 5.1 times larger on Fe_2O_3-AR than on Fe_2O_3-R, respectively. Thus, the increase of the adsorption of these intermediate olefins enhanced the carbon chain growth. In contrast, CO_2 selectivity was almost unchanged (30.5% and 30.6%) despite the regeneration of Fe_3O_4.

In Table 4, the molar flow rate and p/o ratio of C_2-C_4 hydrocarbons in the product stream are listed. Entire paraffin to olefin ratio in the C_2-C_4 range slightly increased from 2.11 to 2.15 after 10 h reaction due to the increase in the C_2H_6/C_2H_4 ratio. In contrast with C_2 hydrocarbons, the p/o ratio in C_3 and C_4 decreased. The

Table 4. Molar flow rate of paraffin and olefin in C_2-C_4 range produced by the Fe_2O_3 catalyst

Catalyst	Time on stream (h)	Moles in the product stream (10^{-6} mol/min)							
		C_2H_6 / C_2H_4	p/o[a]	C_3H_8 / C_3H_6	p/o	C_4H_{10}[b] / C_4H_8	p/o	Paraffin / Olefin	p/o
Fe_2O_3-R	0.5	4.90 / 0.89	5.48	3.01 / 2.52	1.19	1.53 / 1.06	1.44	9.44 / 4.47	2.11
Fe_2O_3-AR	10	5.06 / 0.74	6.84	2.96 / 2.56	1.15	1.48 / 1.12	1.33	9.50 / 4.42	2.15

[a] The molar ratio of paraffin to olefin

[b] Only *n*-C_4H_{10} was detected

re-adsorption of olefin also enhanced the p/o ratio due to the hydrogenation of re-adsorbed olefins [46,47]. Thus, the increase of the adsorption strength of olefin resulted in an increase of p/o ratio. As seen in the TPD results shown in Fig. 3, the adsorption strength of C_2H_4 on Fe_2O_3-AR increased, while that of C_3H_6 decreased, resulting in an increase in ethane and propylene selectivity.

CONCLUSION

The surface properties of an Fe_2O_3 catalyst and their effects on high-calorie SNG production activity were investigated. The active phase of Fe_2O_3 catalyst reduced by CO was a mixture of low-carbon FeC_x and Fe_3C, and these phases were maintained over the 10 h reaction course accompanied by the regeneration of Fe_3O_4. Although the changes in the bulk were slight, the changes on the surface were severe. The surface concentration of Fe increased from 2.3% to 6.7% after 10 h reaction, which enhanced both CO adsorption and the adsorbed amount of light olefins (C_2H_4, C_3H_6), resulting in an increased CO conversion and carbon chain growth, respectively. The surface concentration of oxygen also increased due to the regeneration of Fe_3O_4, which resulted in a reduction in the strength of C_3H_6 adsorption and a decrease in the p/o ratio in C_3 hydrocarbons. In contrast, an increase in the strength of C_2H_4 adsorption resulted in an increase in the p/o ratio in C_2 hydrocarbons. From this result, it is inferred that the predominant hydrocarbon product can be selected by designing the surface composition and the electron density of the catalyst: for example, a lower electron density is preferred for the production of propylene, while a positively charge (or Lewis acidic) surface is preferable for the production of propane.

ACKNOWLEDGEMENTS

This research was supported by C1 Gas Refinery Program through the National Research Foundation of Korea (NRF) funded by the Ministry of Science, ICT & Future Planning (2016M3D3A1A01913252).

This work was supported by the Institutional Program (2E26570-16-036) of the Korea Institute of Science and Technology (KIST).

REFERENCES

1. Statistical Review of World Energy, British Petroleum (2015).
2. The Paris Agreement, in: The Conference of the Parties Twenty-first Session (COP 21), United Nations Framework Convention on Climate Change (UNFCCC) (2015).
3. World Energy Outlook 2015, International Energy Agency (2015).
4. Lower and higher heating values of gas, liquid and solid fuels, Biomass Energy Data Book, U.S. Department of Energy, Oak Ridge National Laboratory (2011).
5. NIST Chemistry Webbook, National Institute of Standards and Technology, Washington, D.C. <http://webbook.nist.gov/chemistry/>.
6. T. Kume and T. Ohashi, Gas quality variation impact on gas appliances in Japan: A status report, 25th World Gas Conference, Kuala Lumpur, Malaysia (2012).
7. Y. Nishiyama, Energy in Japan, Credit Suisse (2012).
8. Heat content of natural gas consumed, U.S. Energy Information Administration (EIA).
9. M. Korchemkin, Gazprom unlikely to win a price war, East European Gas Analysis (EEGA) (2016).
10. Scale Does Matter, Gazprom (2012).
11. C. A. Koh, *Chem. Soc. Rev.*, **31**, 157 (2002).
12. Q. W. Zhang, X. H. Li, K. Asami, S. Asaoka and K. Fujimoto, *Catal. Today*, **104**, 30 (2005).
13. Q. Zhang, X. Li, K. Asami, S. Asaoka and K. Fujimoto, *Catal. Lett.*, **102**, 51 (2005).
14. Q. J. Ge, X. H. Li, H. Kaneko and K. Fujimoto, *J. Mol. Catal. A-Chem.*, **278**, 215 (2007).
15. Q. J. Ge, Y. Lian, X. D. Yuan, X. H. Li and K. Fujimoto, *Catal. Commun.*, **9**, 256 (2008).
16. Q. J. Ge, T. Tomonobu, K. Fujimoto and X. H. Li, *Catal. Commun.*, **9**, 1775 (2008).
17. X. G. Ma, Q. J. Ge, C. Y. Fang, J. G. Ma and H. Y. Xu, *Fuel*, **90**, 2051 (2011).
18. Q. W. Zhang, T. Ma, M. Zhao, T. Tomonobu and X. H. Li, *Catal. Sci. Technol.*, **6**, 1523 (2016).
19. Y. W. Li, D. H. He, Z. X. Cheng, C. L. Su, J. R. Li and Q. M. Zhu, *J. Mol. Catal. A-Chem.*, **175**, 267 (2001).
20. Y. W. Li, D. H. He, Y. B. Yuan, Z. X. Cheng and Q. M. Zhu, *Fuel*, **81**, 1611 (2002).
21. Y. W. Li, D. H. He, Q. M. Zhu, X. Zhang and B. Q. Xu, *J. Catal.*, **221**, 584 (2004).
22. Y. W. Li, D. H. He, Z. H. Zhu, Q. M. Zhu and B. Q. Xu, *Appl. Catal. A-Gen.*, **319**, 119 (2007).
23. Z. H. Zhu and D. H. He, *Fuel*, **87**, 2229 (2008).
24. S. H. Ge, D. H. He and Z. P. Li, *Catal. Lett.*, **126**, 193 (2008).
25. R. J. Zhang, H. M. Liu and D. H. He, *Catal. Commun.*, **26**, 244 (2012).
26. H. M. T. Galvis and K. P. de Jong, *ACS Catal.*, **3**, 2130 (2013).
27. H. M. T. Galvis, J. H. Bitter, C. B. Khare, M. Ruitenbeek, A. I. Dugulan and K. P. de Jong, *Science*, **335**, 835 (2012).
28. H. M. T. Galvis, J. H. Bitter, T. Davidian, M. Ruitenbeek, A. I. Dugulan and K. P. de Jong, *J. Am. Chem. Soc.*, **134**, 16207 (2012).
29. S. H. Kang, J. W. Bae, P. S. S. Prasad and K. W. Jun, *Catal. Lett.*, **125**, 264 (2008).
30. M. E. Dry, FT catalysts, in: A. P. Steynberg, M. E. Dry (Eds.), *Stud. Surf. Sci. Catal.*, 533 (2004).
31. B. C. Enger and A. Holmen, *Catal. Rev.*, **54**, 437 (2012).
32. T. Inui, A. Sakamoto, T. Takeguchi and Y. Ishigaki, *Ind. Eng. Chem. Res.*, **28**, 427 (1989).
33. Y. H. Lee, H. Kim, H. S. Choi, D. W. Lee and K. Y. Lee, *Korean J. Chem. Eng.*, **32**, 2220 (2015).
34. Y. H. Lee, D. W. Lee, H. Kim, H. S. Choi and K. Y. Lee, *Fuel*, **159**, 259 (2015).
35. M. K. Gnanamani, H. H. Hamdeh, W. D. Shafer, D. E. Sparks and B. H. Davis, *Catal. Lett.*, **143**, 1123 (2013).
36. M. Y. Ding, Y. Yang, B. S. Wu, J. Xu, C. H. Zhang, H. W. Xiang and Y. W. Li, *J. Mol. Catal. A-Chem.*, **303**, 65 (2009).
37. E. de Smit and B. M. Weckhuysen, *Chem. Soc. Rev.*, **37**, 2758 (2008).
38. J. W. Kolis, E. M. Holt and D. F. Shriver, *J. Am. Chem. Soc.*, **105**, 7307 (1983).

39. W. C. Wu, Z. L. Wu, C. H. Liang, X. W. Chen, P. L. Ying and C. Li, *J. Phys. Chem. B*, **107**, 7088 (2003).
40. Y. F. Liu, J. J. Luo, M. Girleanu, O. Ersen, C. Pham-Huu and C. Meny, *J. Catal.*, **318**, 179 (2014).
41. S. Logdberg, M. Lualdi, S. Jaras, J. C. Walmsley, E. A. Blekkan, E. Rytter and A. Holmen, *J. Catal.*, **274**, 84 (2010).
42. Y. H. Lee, D. W. Lee and K. Y. Lee, *J. Mol. Catal. A-Chem.*, **425**, 190 (2016).
43. A. V. Naumkin, A. Kraut-Vass, S. W. Gaarenstroom and C. J. Powell, NIST X-ray Photoelectron Spectroscopy Database - NIST Standard Reference Database 20, National Institute of Standards and Technology (NIST) (2012).
44. F. Jiang, L. Zeng, S. R. Li, G. Liu, S. P. Wang and J. L. Gong, *ACS Catal.*, **5**, 438 (2015).
45. M. O. Ozbek and J. W. Niemantsverdriet, *J. Catal.*, **317**, 158 (2014).
46. E. W. Kuipers, I. H. Vinkenburg and H. Oosterbeek, *J. Catal.*, **152**, 137 (1995).
47. G. P. Van der Laan and A. A. C. M. Beenackers, *Catal. Rev.*, **41**, 255 (1999).